

Semi-analytical fault injection model: effect of fault roughness and injection scheme on induced seismicity

Thibault Candela¹, Jean Paul Ampuero², Jan Diederik Van Wees¹, Peter Fokker¹, Brecht Wassing¹

¹ TNO Applied Geosciences, P.O. Box 80015, 3508 TA Utrecht, Netherlands

² Université Côte d'Azur, IRD, CNRS, Observatoire de la Côte d'Azur, Géoazur, Sophia Antipolis, France

thibault.candela@tno.nl

Keywords: induced seismicity, fault roughness

ABSTRACT

Our newly developed fault injection model for induced seismicity in the context of geothermal systems starts from the most constrained heterogeneous ingredient of the rupture model, that is the geometrical roughness of fault surfaces.

Synthetic fractal surfaces mapping real fault geometry are combined with an “instantaneous” slip-weakening model with spatially homogeneous static and dynamic friction coefficients.

Without introducing unconstrained frictional heterogeneities, multiple rupture events following the expected dynamic in terms of spatio-temporal distribution are generated. This rich seismicity's dynamic emerges from the non-trivial interplay between pore pressure diffusion, geometrical heterogeneities of the fault surfaces and stress interactions between the successive rupture events.

1. INTRODUCTION

Faults in geothermal systems are often very beneficial for heat-flow improvement. However, they may also pose a threat because of the risk of inducing large earthquakes. The goal is to take advantage of fault conductivity while keeping seismicity in the safe range of low-magnitude events (Zang et al., 2013).

Our present contribution focuses on the induced seismicity aspect. Instead of modelling an entire fault system as many previous works did (Taron et al., 2009; Izadi and Elsworth, 2010; McClure and Horne, 2010), we model induced seismicity for a single-fault injection. This approach is justified by the fact that flow is often concentrated in a couple of faults instead of being homogeneously distributed.

Fault injection models have already been developed (e.g. Mossop, 2001; Catalli et al., 2008; Baisch et al., 2010; Candela et al., 2018). These models can be divided into three classes. The first class derived seismicity in terms of effective behavior and single rupture events are not explicitly modelled (Mossop, 2001; Candela et al., 2018). The second class explicitly generates each single rupture event but often an

engineering approach with unconstrained physical parameters is followed for e.g. either the frictional properties or the stress interactions between rupture events (Catalli et al., 2008; Baisch et al., 2010). The third class is physics-based but focuses on one single rupture event (Galis et al., 2017; 2019).

We present here a newly developed semi-analytical approach which honors the physics of the problem while explicitly modelling multiple successive rupture events. The key in our approach is to focus on the most constrained heterogeneous ingredient of faults, which is their geometrical roughness.

2. MODEL DESCRIPTION

Our goal is to model multiple rupture events induced by injection into a single fault (figure 1). We only account for the direct pressure effect reducing the effective normal stress; poro-elastic and thermo-elastic effects are thus neglected.

To model injection into a single fault, we employ the axisymmetric flow model developed by Mossop (2001). In a radially symmetric system, the diffusion equation can be solved analytically (see Candela et al., 2018 for more details about the derivation). The pore pressure distribution in the fracture is a function of radial distance from the injection point and of time, and it reads

$$p(r, t) = \frac{\dot{m}_{r_b} \eta}{4\pi \rho_w k h} E_1 \left(\frac{r^2}{4c_D t} \right) + p_0 \quad (1)$$

where E_1 is the exponential integral of the first kind, p_0 is the initial pore pressure, r_b the borehole radius, \dot{m}_{r_b} the mass injection rate at the borehole wall, h the fracture thickness, c_D represents the fracture hydraulic diffusivity, η and ρ_w are respectively the water dynamic viscosity and density, and k is fracture permeability (input values are given in table 1).

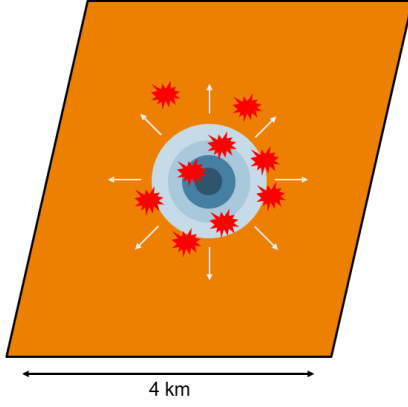


Figure 1. Schematic of the model's intentions.

Pressure model	
r_b	0.1 m
c_D	$1 \text{ m}^2 \text{ s}^{-1}$
h	0.001 m
η	$10^{-3} \text{ kg m}^{-1} \text{ s}^{-1}$
k	10^{-10} m^2
ρ_w	1000 kg m^{-3}

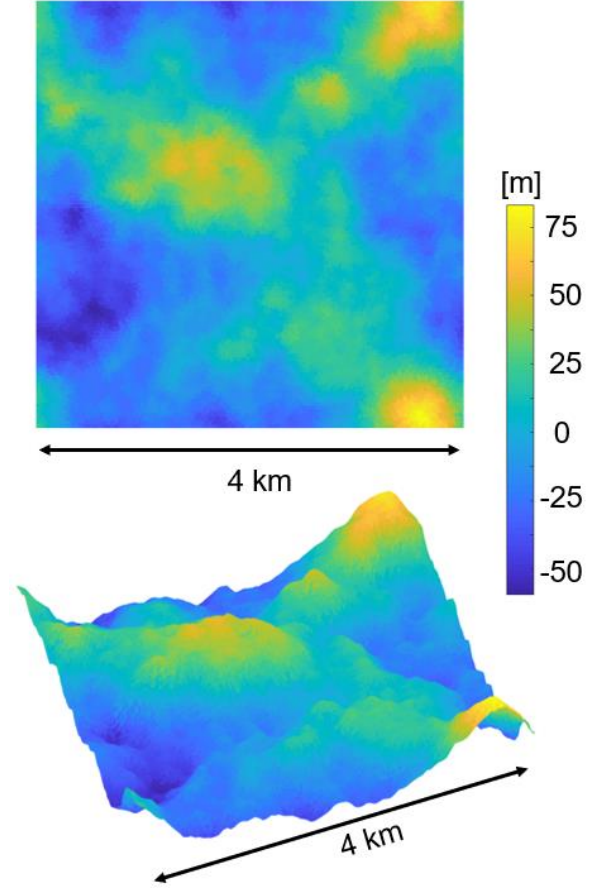
Table 1. Input parameters used for the pressure model.

The key in our modelling approach is to include heterogeneities solely at the level of the fault surface roughness. Indeed, all other model parameters are kept spatially homogenous along the fault surface. Our motivation to focus on fault roughness is two-fold: (1) the characteristics of the fault roughness are well constrained from natural observations, (2) up to date the interplay between fault roughness and multiple rupture events is still unknown.

We generated synthetic fractal self-affine fault surfaces (figure 2) using the method developed in Candela et al. (2009). The standard deviation of the height fluctuations (H) with respect to a planar surface can be described by a power law:

$$H = \beta L^\zeta \quad (2)$$

where L is the length scale of observation along the fault, the pre-factor β defines the roughness amplitude at a reference length scale, and the exponent ζ defines the self-affine scaling properties of the fault surface. For natural fault surfaces, the exponent ζ takes values between 0.6 and 0.8. A narrow range is also observed for the pre-factor $0.1\% \leq \beta \leq 1\%$ (Candela et al., 2012; Brodsky et al., 2016).

Figure 2. Synthetic self-affine fault surface with $\beta = 1\%$ and $\zeta = 0.6$.

We employ a boundary element method to compute stress changes and slip along the fault surface. In order to follow geometrical irregularities of the synthetic fault surfaces, the surface is discretized by a triangular mesh.

To avoid introducing unconstrained complexities in the fault friction, we follow a simple “instantaneous” slip-weakening model and keep a spatially homogenous static and dynamic friction coefficient (figure 3).

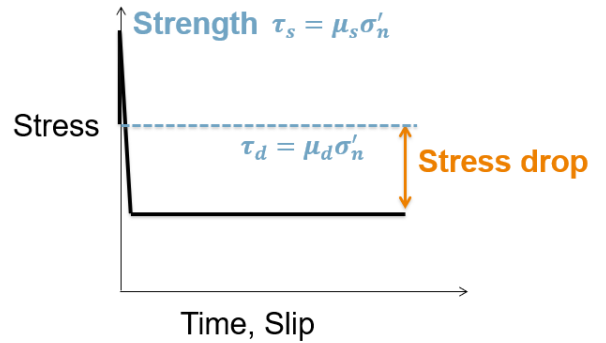


Figure 3. “Instantaneous” slip weakening model.

The frictional strength is defined as:

$$\tau_s = \mu_s \sigma'_n \quad (3).$$

Once this value is reached for one triangular element of the fault surface, the stress drops instantaneously to:

$$\tau_d = \mu_d \sigma'_n \quad (4)$$

The effective normal stress σ'_n reads :

$$\sigma'_n = \sigma_n - p \quad (5)$$

where σ_n is the total normal stress, and p the pore pressure defined in equation (1). μ_s and μ_d are respectively the static and dynamic friction coefficients. For all the results presented in this manuscript we used $\mu_s = 0.65$ and $\mu_d = 0.6$. We assume instantaneous frictional healing after each event (the friction coefficient is reset to its original static value).

During each rupture event, elastic stress interactions between the fault elements are accounted for via elastic Green’s functions for triangular dislocations (Nikkhoo and Walter, 2015). Coupling the Barnes-Hut algorithm (Barnes and Hut, 1986) with hierarchical matrices (Bradley, 2014) can significantly speed up this step and enables multiscale analysis.

3. RESULTS

For all the simulations, the roughness of the fault surfaces is characterized by a unique Hurst exponent $\zeta = 0.6$; and given the selected pre-factors, two fault-type are defined: (1) the “rough” faults with $\beta = 1\%$ and (2) the “smooth” faults with $\beta = 0.1\%$.

3.1 Pre-stress distribution

As a first initialization phase, we aim to recover the appropriated pre-stress distribution before the onset of injection. This distribution is thought to be controlled by the non-trivial interaction between fault roughness and millions of successive tectonic events.

Each of the modelled vertical strike-slip fault is placed in the same uniform strike-slip tectonic regime. The faults are placed in the same remote stress tensor and loaded by the same remote stress rate tensor. However, the resolved shear and normal stress and stress rate on each fault element depend on its orientation relative to the overall fault orientation.

In order to avoid pathological growths of stress at geometric irregularities (Duan and Oglesby, 2005; 2006; Dunham et al., 2011; Fang and Dunham, 2013), each fault elements adheres to a viscoelastic-type rheology as proposed by Nielsen and Knopoff (1998):

$$\tau(i, t) = \left(\tau(i, 0) - \left(\eta \frac{\tau_r(i)}{G} \right) \right) \exp \left\{ -t \frac{G}{\eta} \right\} + \eta \left(\frac{\tau_r(i)}{G} \right) \quad (6)$$

$$\sigma(i, t) = \left(\sigma(i, 0) - \left(\eta \frac{\sigma_r(i)}{G} \right) \right) \exp \left\{ -t \frac{G}{\eta} \right\} + \eta \left(\frac{\sigma_r(i)}{G} \right) \quad (7)$$

where $\tau(i, 0)$, $\sigma(i, 0)$, $\tau_r(i)$ and $\sigma_r(i)$ are respectively the local initial shear stress, initial normal stress, shear stress rate, and normal stress rate for each fault element

i. The viscosity η and shear modulus G are kept spatially uniform and constant for all the simulations.

At steady state, equation (6) and (7) reduce to :

$$\tau_{ss}(i) = \frac{\eta}{\mu} \tau_r(i) \quad (8)$$

$$\sigma_{ss}(i) = \frac{\eta}{\mu} \sigma_r(i) \quad (9)$$

At steady state, the effective friction $\mu_e = \tau_{ss}(i)/\sigma_r(i)$ is thus solely controlled by the ratio:

$$\mu_e(i) = \tau_r(i) / \sigma_r(i) \quad (10)$$

It results that the effective friction is thus solely dependent on the fault roughness. However, the contribution of the rupture events and successive stress distributions on the effective friction still need to be added.

Figure 4 presents the evolution of the effective friction during the initialization phase. After millions of successive tectonic rupture events, the effective friction reaches its steady state. The mean effective friction (average over all fault elements) solely controlled by the fault roughness (i.e. as defined by equation (10)) is very close to the simulated mean effective friction including the effect of the successive rupture events. The mean effective friction is slightly lower for the “rough” fault, but its standard deviation is significantly larger than that of the “smooth” fault.

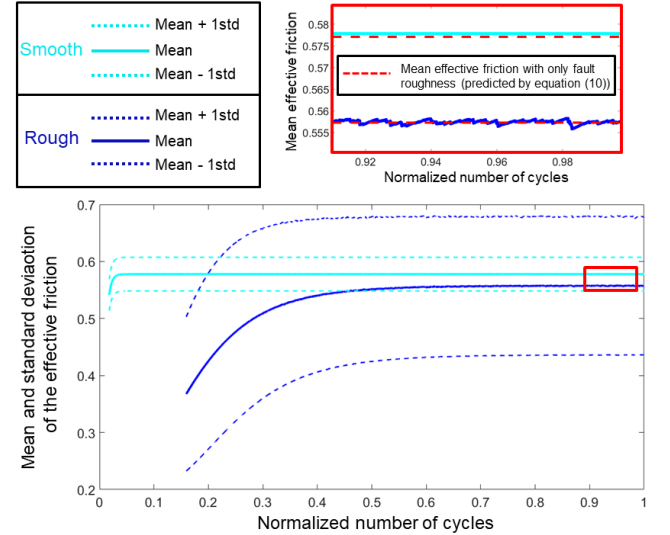


Figure 4. Evolution of the effective friction during the initialization phase. The small black rectangle on the bottom’s graph corresponds to the location of the magnified graph on the top.

At steady state, the modelled earthquake magnitude distribution (see figure 5) follows a pareto-type power law distribution as observed for both tectonic and induced events.

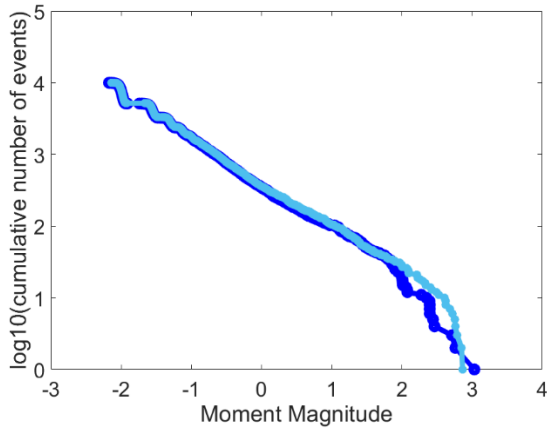


Figure 5. Magnitude-size distribution for two “rough” type faults with two different random phases.

3.2 Injection-induced seismicity

The pre-stress distributions obtained at steady state at the end of the initialization phased are now used as input for the injection-induced seismicity modelling.

Two injection schemes have been tested. One fast scheme where 2000 m³ is injected at 10 l/s during 2.5 days; and one slow scheme where 2000 m³ is injected at 1 l/s during 25 days. For both schemes an additional shut-in phase of 30 days is modelled. Figure 6 presents the distribution of the change in pore pressure for the fast injection scheme.

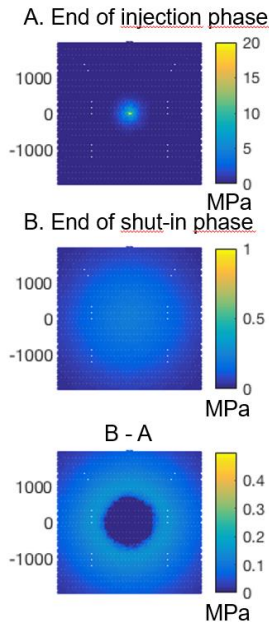


Figure 6. Distribution of the change in pore pressure for the fast injection scheme. The bottom panel is the difference between the change in pore pressure at the end of the shut-in phase and the change at the end of the injection phase. This panel highlights the diffusion-driven fluid pressure distribution during the shut-in phase: (1) the decay in fluid pressure close to the injection well, and (2) and its slow increase at distant radius.

Figures 7 and 8 display the output in terms of seismicity distribution and its relationship with the fluid pressure disturbance.

For both the two fault-types (“rough” and “smooth”) and the two injection schemes, two key observations can be made: (1) the seismicity persists long after during the shut-in period; (2) rupture events nucleate at large distance from the injector where the change in fluid pressure is less than 0.1MPa.

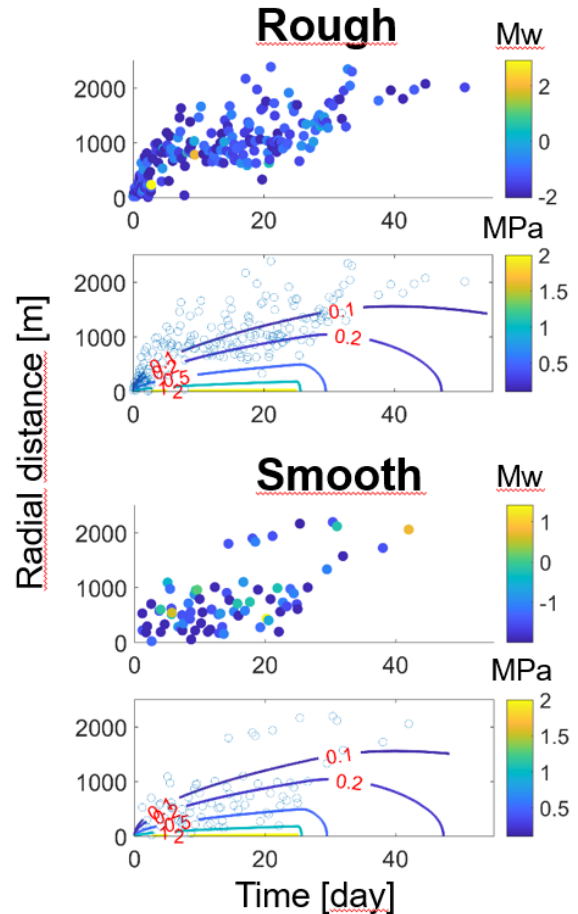


Figure 7. Slow injection scheme: spatio-temporal distribution of the induced seismicity and changes in pore pressure. For each fault-type (“rough” and “smooth”), the top and bottom panel display respectively the seismicity magnitude and the changes in pore pressure.

The “rough” fault hosts more induced events relatively to the “smooth” fault. Consequently, the seismicity’s persistence along the “rough” fault is more severe (i.e. more events) and lasts longer relatively to the “smooth” fault.

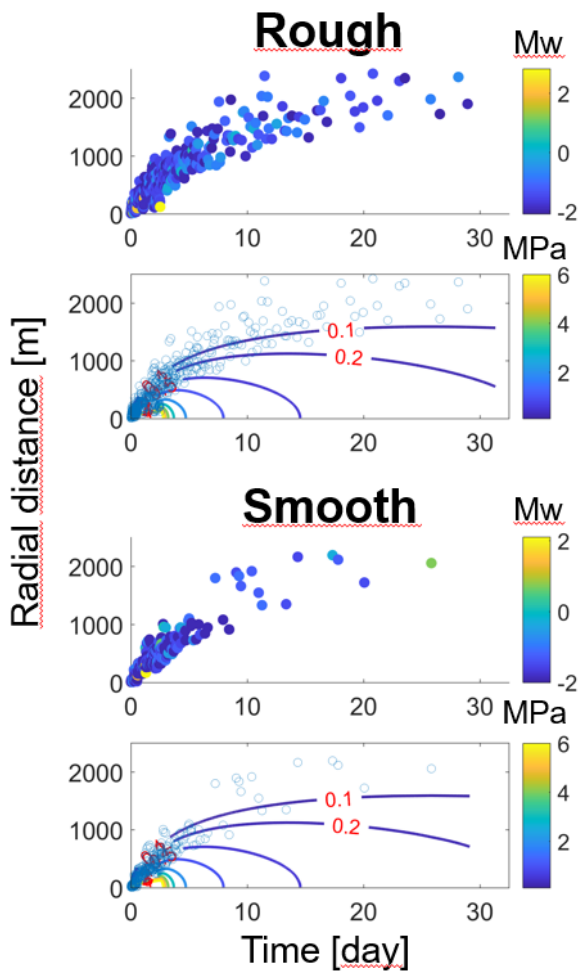


Figure 8. Fast injection scheme: spatio-temporal distribution of the induced seismicity and changes in pore pressure. For each fault-type (“rough” and “smooth”), the top and bottom panel display respectively the seismicity magnitude and the changes in pore pressure.

4. DISCUSSIONS - CONCLUSIONS

We presented a physic-based fault-injection model allowing to model multiple rupture events along 3D fractal self-affine fault surfaces.

From solely the geometrical heterogeneities of the fault roughness emerges a rich seismicity dynamics as observed: (1) for tectonic and induced earthquakes, and (2) in previous modelling results accounting for frictional heterogeneities.

A clear difference in terms of induced seismicity is observed between the “rough” and “smooth” faults. These two end-members in terms of fault roughness amplitude are consistent with the ones observed for natural fault surfaces. More induced events nucleate along rough faults. The pre-stress distribution obtained from the first initialization phase is probably playing a role at this level.

Induced events are modelled at large distances from the injector. Honoring the geometrical heterogeneities can thus produce outcomes similar to those expected: (1)

when introducing poro-elastic effects, or when using an ETAS statistical approach to model aftershocks.

However, for now we refrain ourselves in terms of interpretation since a more probabilistic approach is required. This is what we plan to do next. Indeed, our modelling approach is computationally fast and offers the opportunity to explore multiple scenarios and to condition model parameters with data.

Acknowledgements

The project leading to part of the results in this article received funding from the European Union’s Horizon 2020 research and innovation programme under grant agreement No 691728

REFERENCES

- Baisch, S., Vörös, R., Rothert, E., Stang, H., Tischner, T., and R. Schellschmidt: A numerical model for fluid injection induced seismicity at Soultz-sous-Forêts. *Int. Jour. Rock Mech. Min. Sci.*, (2009) doi:10.1016/j.ijrmms.2009.10.001.
- Barnes, J. and Hut, P.: A Hierarchical $O(N \log N)$ force calculation algorithm, *Nature*, (196) 324, 446 pp., 1986.
- Bradley, A.M. Software for efficient static dislocation-traction calculations in fault simulators, *Seis. Res. Lett.*, 85(6), 2014, doi:10.1785/0220140092.
- Brodsky, E.E., J. Kirkpatrick and T. Candela, Constraints from fault roughness on the scale-dependent strength of rocks, *Geology*, (2016) 44(1), 19-22, DOI:10.1130/G37206.1.
- Candela, T., F. Renard, Y. Klinger, K. Mair, J. Schmittbuhl and E.E. Brodsky, Roughness of fault surfaces over nine decades of length scales, *J. Geophys. Res.*, (2012), 117, B08409, DOI:10.1029/2011JB009041.
- Candelat T., van der Veer, E.F., Fokker, P.A., On the importance of thermo-elastic stressing in injection-induced earthquakes, *Rock Mechanics and Rock Engineering* (2018), 51 (12), 3925-3936.
- Catalli, F., Cocco, M., Console, R., Chiaraluce, L., Modeling seismicity rate changes during the 1997 Umbria-Marche sequence (central Italy) through a rate and state-dependent model. *J. Geophys. Res. Solid Earth.*, (2007) doi:10.1029/2007JB005356.
- Duan, B. and Oglesby, D. D. Multicycle dynamics of nonplanar strike-slip faults, *J. Geophys. Res.* (2005), 110, B03304.
- Dunham, E. M., D. Belanger, L. Cong, and J. E. Kozdon, Earthquake ruptures with strongly rate-weakening friction and off-fault plasticity, 2: Nonplanar faults, *Bulletin of the Seismological*

- Society of America*, (2011), 101(5), 2308-2322, doi:10.1785/0120100076.
- Galis, M., J. P. Ampuero, P. M. Mai and F. Cappa
Induced seismicity provides insight into why
earthquake ruptures stop
Science Advances, (2017) 3 (12), eaap7528,
doi:10.1126/sciadv.aap7528
- Galis, M., J. P. Ampuero, P. M. Mai, J. Kristek,
Initiation and arrest of earthquake ruptures due to
elongated overstressed regions
Geophys. J. Int., (2019)
doi:10.1093/gji/ggz086/5322168
- Izadi, G., Elsworth, D. The influence of thermal-
hydraulic-mechanical-and chemical effects on the
evolution of permeability, seismicity and heat
production in geothermal reservoirs. *Geothermics*.
(2015) Vol 53. pp. 385-395.
- McClure, M.W., Horne, R.N. Discrete Fracture
Modeling of Hydraulic Stimulation in Enhanced
Geothermal Systems. Proceedings, *Thirty-Fifth
Workshop on Geothermal Reservoir*. (2010).
- Mossop, A., Injection Induced Seismicity: A
thermoelastic model, *Ph.D. thesis*, chapter 5,
(2001),
(<https://pangea.stanford.edu/cdfm/sites/default/files/pubs/mossop2001ch5.pdf>).
- Nikkhoo, M., Walter, T. R. Triangular dislocation: an
analytical, artefact-free solution. - *Geophysical
Journal International*, (2015). 201 (2), 1117-1139.
doi:10.1093/gji/ggv035.
- Nielsen, S. B. and Knopoff, L. The equivalent strength
of geometrical barriers to earthquakes, (1998) *J.
Geophys. Res.-Sol. Earth* 103, 9953–9965.
- Taron, J. Elsworth, D., Min, K.-B. Numerical
simulation of thermal-hydrologic mechanical-
chemical processes in deformable fractured porous
media. (2009) *Int. J. R. Mechs.* Vol. 46, pp. 842-
854.
- Zang, A., Seok Yoon, J., Stephansson, O., Heidbach,
O., Fatigue hydraulic fracturing by cyclic reservoir
treatment enhances permeability and reduces
induced seismicity. (2013). *Geophys. J. Int.* doi:
10.1093/gji/ggt301.